



OPEN

Regional subsidence monitoring and prediction along high-speed railways based on PS-InSAR and LSTM

Yong-An Xue^{1,2}✉, You-Feng Zou^{1,3}, Hai-Ying Li⁴ & Wen-Zhi Zhang^{1,3}

The rapid construction of high-speed railways in China has forced more and more routes to pass through slow subsidence zones caused by groundwater extraction or underground mining. It is crucial to carry out deformation monitoring and prediction those areas along high-speed railways to ensure the safe operation. Twenty-nine periods of Sentinel-1A data between Taiyuan South Station and Taigu East Station were first processed using the PS-InSAR technique, and the ground subsidence sequences at ten typical points were selected. Then the Variational modal decomposition (VMD) was combined with the Adaptive Boosting Algorithm (AdaBoost), and the VMD-LSTMAda-LSTMAda model was constructed by combining the long short-term memory (LSTM) model for the prediction of regional ground subsidence along the high-speed railway. The results show that the cumulative subsidence within the 200 m buffer of the line centreline is $-37.58\text{--}89.19$ mm, and the annual average subsidence rate is $-26.57\text{--}82.63$ mm/y. The proposed model can reduce the complexity of the deformation sequence and combines with AdaBoost to improve the prediction accuracy of the LSTM model. It performs well in terms of RMSE, MAE, MAPE, and R^2 at the two feature points (3703: RMSE = 0.82 mm, MAE = 0.25 mm, MAPE = 6.31%, and R^2 = 0.94; 522: RMSE = 1.32 mm, MAE = 0.46 mm, MAPE = 4.92%, R^2 = 0.95). The model improves the accuracy of regional subsidence prediction along the high-speed railway.

High-speed railway foundation subsidence deformation monitoring and control is very important for its high reliability, high stability, and high smoothness in operation¹. At present, there are many de-formation monitoring technology methods, both based on traditional optical instruments (precision level measurement²) and electronic instruments (total station³, measurement robot⁴, GNSS⁵, liquid static level measurement⁶) for periodic observation and analysis, and also based on InSAR^{7,8}, LiDAR⁹, and GNSS continuous operation reference station¹⁰, 3D laser scanning¹¹, fiber optic sensing¹² and other modern mapping techniques for deformation monitoring, and multi-source collaborative monitoring that integrates multiple observation techniques^{13,14}, which provide abundant technical references for the monitoring of the foundation subsidence of high-speed railways.

Although the concept of InSAR technology has been proposed for several decades, its recent advancements have made it particularly suitable for surface deformation monitoring. This is attributed to its capabilities of all-weather operation, real-time monitoring, high efficiency, and the ability to cover large-scale areas under study¹⁵⁻¹⁷. Due to their characteristics, such as large spans, extensive coverage, and the need to operate under complex and variable natural conditions, high-speed railways and other linear infrastructures pose unique challenges for deformation monitoring. In this context, the use of Interferometric Synthetic Aperture Radar (InSAR) offers significant advantages, including cost-effectiveness and the ability to identify regional subsidence centers along the railway lines. These benefits are unmatched by other monitoring methods, which often struggle to provide the same level of detail and coverage^{18,19}. Permanent Scatterers Interferometry (PS-InSAR) is an advanced technique that has emerged subsequent to the development of Differential Interferometric Synthetic Aperture Radar (D-InSAR)²⁰, which is based on the comprehensive analysis of multiple images in the study area, the deployment of the network, the establishment of a model of the phase difference between two adjacent points as a function of the rate of deformation and elevation correction, the separation of the phase components, and

¹School of Surveying and Land Information Engineering, Henan Polytechnic University, Jiaozuo 454000, China.

²College of Mining Engineering, Taiyuan University of Technology, Taiyuan 030024, China. ³Henan Engineering Research Center for Ecological Restoration and Construction Technology of Goaf Sites, Jiaozuo 454000, China.

⁴Shanxi Geological Group Testing Technology Co., Taiyuan 030001, China. ✉email: xueyongan@tyut.edu.cn

the final extraction of the deformation components²¹. InSAR technique has significantly better deformation monitoring accuracy than the D-InSAR technique, and can be applied to deformation monitoring in low-coherence areas with strong advantages, which has gained extensive attention and research from many scholars^{22,23}, and has been widely used in deformation monitoring of linear projects such as subways, highways, and high-speed railways^{24–26}. Ge et al. used radar interferometry (including D-InSAR and PS-InSAR) to acquire and analyze the possible ground deformation along the Beijing-Tianjin high-speed railway and cross-validated the ALOS D-InSAR results with the ENVISAT PS-InSAR results, which provided a methodological reference for the analysis of high-speed railways subject to surface subsidence²⁷. You et al. selected the updated SBAS-InSAR technique to process and analyze the 35-view Sentinel-1A SAR data, and obtained the subsidence rate and subsidence sequence values along the Panying Railway Passenger Dedicated Line and the Harbin-Dalian Railway Passenger Dedicated Line, which provide an exploration of the application of the InSAR technique for the monitoring of the subsidence of the high-speed railway line²⁸.

The Taiyuan-Jiaozuo High-speed Railway (TJHR), a crucial link between Taiyuan City in Shanxi Province and Jiaozuo City in Henan Province, forms a vital segment of the "Hohhot-South Passage Road," a key component of the "Medium and Long-Term Railway Network Plan" (2016 edition). Groundwater overexploitation in the Taiyuan Basin, situated at the heart of Shanxi Province, has resulted in a persistent drop in groundwater levels, triggering ground subsidence within the basin. This phenomenon poses a potential hazard to the safe operation of the TJHR in the area. Presently, a growing body of literature employs In-SAR technology to investigate ground subsidence in the Taiyuan basin^{29–31}. Tang et al. utilized Sentinel-1 satellite data from 2015 to 2020 for time series SBAS-InSAR processing in the basin, revealing a – 70.0 mm/a subsidence rate in the central Taiyuan basin area encompassing Xiaodian-Qingxu-Jiaocheng-Qixian-Taigu³². They observed distinct "subsidence-bounce" characteristics influenced by seasonal groundwater level fluctuations, with annual cyclic deformation reaching 26.2 mm. These studies offer valuable insights for monitoring ground subsidence along the TJHR³³.

Predicting deformation sequences derived from deformation monitoring techniques holds significant importance for evaluating high-speed railway safety, as well as disaster prevention and mitigation. The Long Short-Term Memory (LSTM) model³⁴, a specialized Recurrent Neural Network (RNN) architecture addressing long-term dependency and gradient issues in RNNs, has garnered considerable attention for its prowess in sequence data prediction^{35–37}. Ye et al. utilized the PS-InSAR technique to capture long-term deformation trends in Zhengzhou city, analyzing ground subsidence patterns along the metro line³⁸. They developed a multi-point ground subsidence prediction model using LSTM to forecast subsidence at a typical metro station. However, inherent limitations of the LSTM model suggest the potential for enhancement through comprehensive training using the AdaBoost algorithm³⁹ to create the LSTM-AdaBoost robust prediction model, thereby boosting LSTM prediction accuracy^{40,41}. Dragomiretskiy and Zosso introduced the Variational Modal Decomposition (VMD) method, a signal decomposition approach based on adaptive signal decomposition, iteratively identifying Intrinsic Mode Functions (IMF) representing local frequency characteristics⁴². By decomposing the subsidence sequence along the high-speed railway into smooth IMF sub-sequences using VMD, and subsequently combining these sub-sequences into trend and disturbance terms based on frequency, followed by individual predictions using the integrated LSTM-AdaBoost model, an improvement in deformation prediction accuracy and reliability can be theoretically achieved. Current research emphasizes decomposition pre-diction and subsequent combination methods^{43–48}. Wang et al. merged Empirical Mode Decomposition (EMD) with Gradient Boosting Decision Tree (GBDT) methods (EMD-GBDT) to forecast land subsidence along high-speed railways, offering valuable insights for similar studies⁴⁹.

The prediction of deformation in high-speed railway areas prone to subsidence is challenged by the nonlinear and non-stationary characteristics of deformation sequences, which introduce uncertainty in the reliability of time series prediction models. Although the LSTM model has seen some application, it has not addressed the prediction lag issues stemming from its inherent model limitations. In this study, we propose a novel predictive approach that leverages the concept of 'decomposition-forecasting-combination'. The VMD is employed to reduce the non-stationarity of deformation sequences and enhance the predictive performance of individual models through ensemble training. Specifically, a combined forecasting method is introduced that utilizes time series InSAR technology to acquire deformation sequences as a training set, integrating VMD with an ensemble boosting method, AdaBoost. Initially, the subsidence series derived from the PS-InSAR solution undergoes decomposition into relatively smooth IMF subsequences utilizing the VMD technique, leading to the creation of a perturbation term and a trend term. Subsequently, the LSTM model undergoes training through AdaBoost integration. Following this, the trained LSTM-AdaBoost model is employed to predict the perturbation term and trend term individually, with the overall prediction result being a weighted average of the predictions.

Results

Regional deformation characteristics

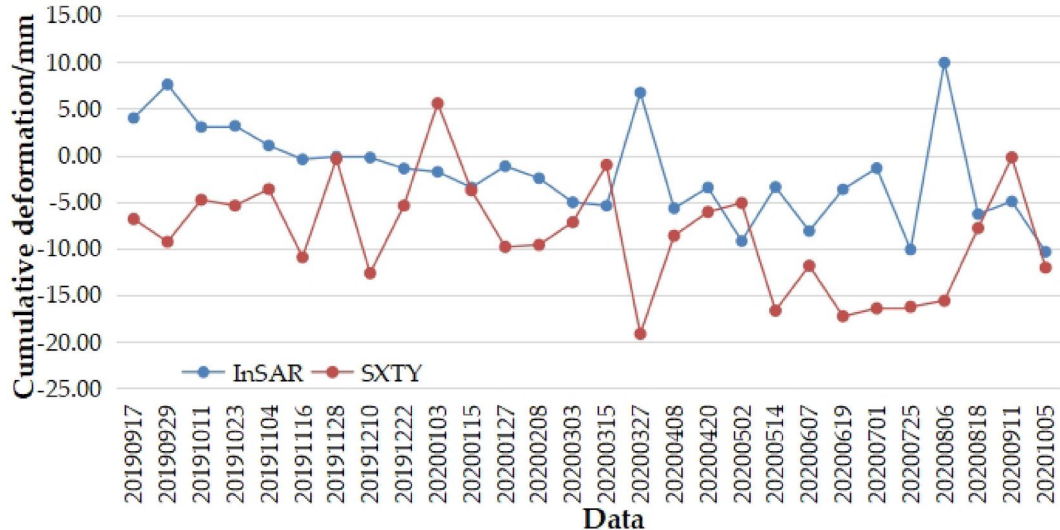
The two images of the study area were mosaicked, and the differential interference phase of the PS point target was obtained by differential interference processing, then the deformation rate of the PS point was finally obtained by a series of operations such as interferogram calculation. Among them, the threshold value of the PS point was selected as 0.75 by using the amplitude stability coefficient method.

Accuracy verification

The radar line-of-sight direction monitoring results were converted to vertical di-rection and then compared with the land-state network GNSS monitoring results, the radar line-of-sight direction converted to vertical direction is calculated as:

$$\Delta d' = \Delta d / \cos \theta \quad (1)$$

Number	V(mm/y)	VLOS (mm/y)	Absolute error (mm/y)
SXTY	-2.44	-2.59	0.15
SXYC	8.54	7.97	0.57

Table 1. Comparison of PS-InSAR and land-state network GNSS continuously operating stations.**Fig. 1.** A comparison of the cumulative deformation results from PS-InSAR monitoring with the GNSS continuous observation at the SXTY site.

where, $\Delta d'$ is a vertically oriented shape variable. Δd is the radar line-of-sight direction variant. θ is the radar angle of incidence. The annual mean deformation rate V of InSAR corresponding to the SXTY and SXYC site were extracted by Kriging interpolation of the twelve surrounding PS points, which were transformed into the vertical annual mean deformation rate VLOS for comparison with the V of GNSS. As shown in Table 1, the V derived from GNSS data and the VLOS obtained from InSAR monitoring at the SXTY site between 5 September 2019 and 5 October 2020 are -2.44 mm/y and -2.59 mm/y , respectively. The discrepancy between these values is 0.15 mm/y . In contrast, at the SXYC station, the difference is 0.57 mm/y . The trend of change in the InSAR monitoring outcomes aligns with that of the terrestrial network monitoring results.

A comparison of the cumulative vertical deformation between the SXTY and SXYC stations is depicted in Figs. 1 and 2.

Figures 1 and 2 indicate that the overall trend of the time series obtained from PS-InSAR monitoring at the SXYC station is approximately similar, but significant differences were observed on January 3, 2020, and June 19, 2020. The goodness of fit for time series monitoring at the SXTY station, when compared with the PS-InSAR monitoring results, is somewhat less consistent than that of the SXYC station, yet the general trend remains aligned, with a notable divergence occurring on March 27, 2020. These discrepancies are likely closely related to meteorological factors and interpolation errors on the day of observation, impacting the monitoring results for a specific period, but not affecting the overall deformation trend. By the end of the monitoring period, the cumulative deformation values were essentially consistent. Integrating Table 1 and Figs. 1 and 2, the results are highly reliable and can be utilized for characterizing the deformation of the research subject and for the training and validation of the predictive model presented in this study.

Annual mean surface deformation characteristics

The twenty-nine periods of high-precision surface deformation results obtained by the PS-InSAR technique for the study area from 5 September 2019 to 5 October 2020 are shown in Fig. 3. It shows that the PS points are mainly located on stable scatterers such as villages, buildings, and roads in the Taiyuan Basin, while they are sparsely distributed in the western mountainous areas due to the influence of vegetation cover, and also less distributed on the cultivated land in the Taiyuan Basin, which makes the selection of PS points reliable. Based on the deformation rate of each PS point, Kriging interpolation was used to obtain the V map of the study area shown in Fig. 4. The ground subsidence pattern in Fig. 4 is consistent with that in Fig. 3, but there is a phenomenon of significantly larger deformation rate in the southeast part of Qingxu, which can be seen in the local image after superimposing PS points and zooming in, which is due to the scarcity of identified PS points in the area, resulting in the amplification of the interpolated deformation rate, which is also a shortcoming of the PS-InSAR technology in the suburbs of the towns and rural areas.

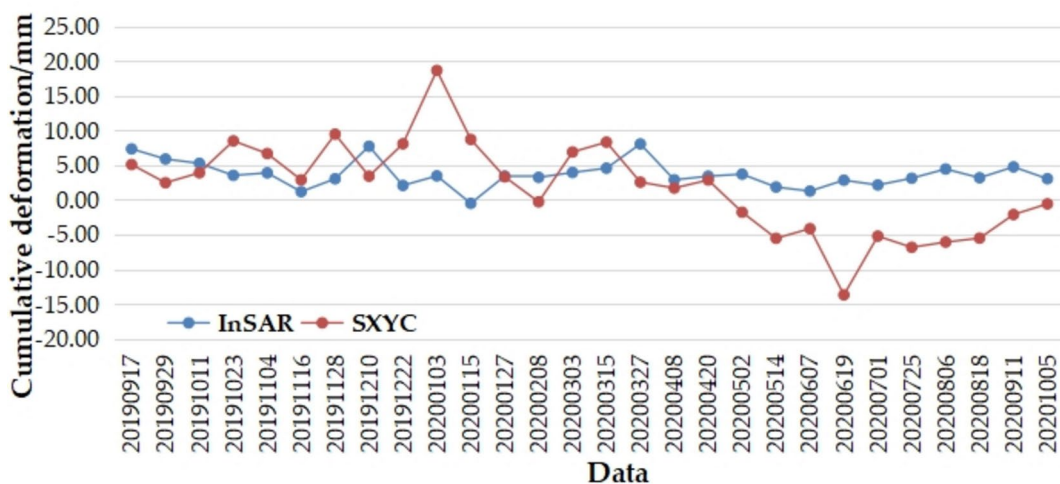


Fig. 2. A comparison of the cumulative deformation results from PS-InSAR monitoring with the GNSS continuous observation at the SXYC site.

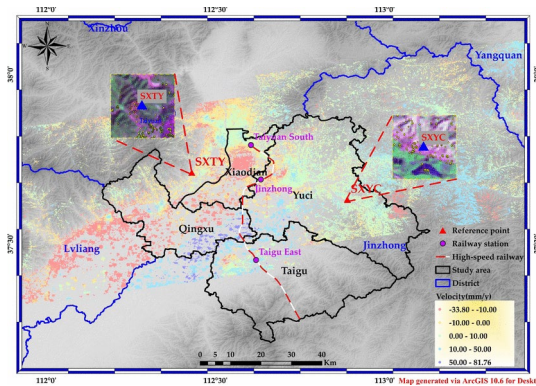


Fig. 3. Spatial distribution of validation points.

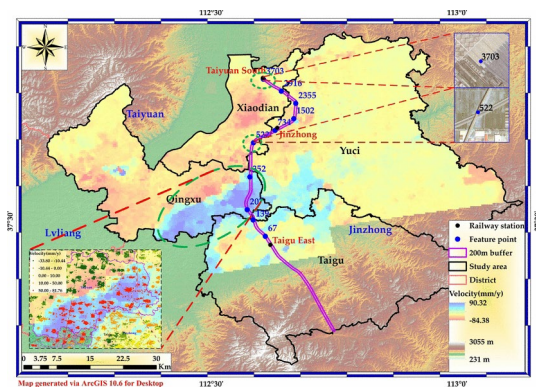


Fig. 4. Annual average surface deformation rate in the study area.

Cumulative surface deformation characteristics of feature points

To better grasp the surface deformation characteristics along the high-speed rail line, a buffer of 200 m was built between Taiyuan South Railway Station and Taigu East Railway Station to the left and right with the center line of the line, and ten PS points were selected as feature points in the buffer zone (Fig. 4), with the point numbers of 67, 139, 207, 352, 522, 734, 1502, 2355, 2916, and 3703 respectively, of which, No. 522 was located on the Jinzhong Special Bridge bridge deck roadbed of TJHR, and all other points are located on the buildings

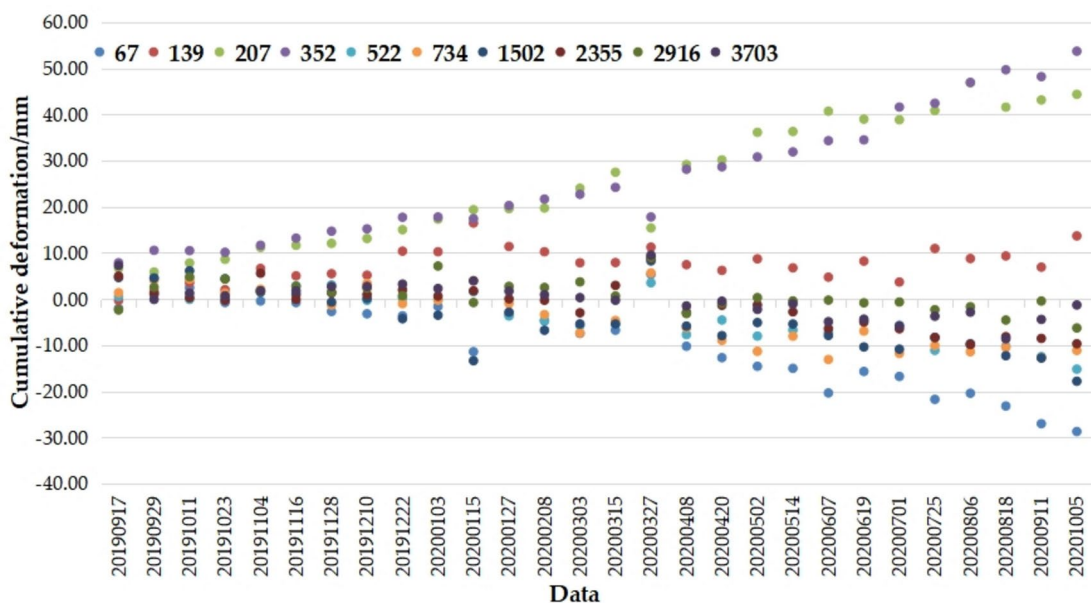


Fig. 5. Cumulative deformation trend of feature points.

Number	67	139	207	352	522	734	1502	2355	2916	3703
Average annual rate of deformation(mm/y)	-19.19	14.48	49.74	50.54	-7.38	-8.23	-9.14	-3.19	1.48	-0.19
cumulative variable(mm)	-28.71	13.67	44.36	53.70	-15.20	-11.15	-17.82	-9.70	-6.28	-1.29

Table 2. Average annual deformation rate and cumulative deformation at feature points.

(structures) and roads along the foundations of the TJHR. The trend of cumulative deformation overtime at the ten feature points during the observation period was obtained (Fig. 5), and the V and cumulative deformation were statistically obtained as shown in Table 2. The annual average deformation rates of the ten feature points ranged from -19.19 to 50.54 mm/y, and the cumulative deformations ranged from -28.71 to 53.70 mm.

Feature point deformation prediction

PS points 3703 and 522 were selected to represent the foundation feature points and roadbed feature points of the TJHR, respectively, and the deformation sequences obtained from PS-InSAR solving between 5 September 2019 and 5 October 2020 were used to make predictions.

Optimal model parameters

The deformation sequence was divided into a training set (70% before the sequence) and a test set (30% after the sequence) for model training and prediction validation respectively. To compare the prediction results objectively and reliably with each other, the optimal parameters of BP, LSTM, and VMD models were determined after a large number of experimental comparisons. Among them, the step size was all taken as 4, the learning rate of the BP model was 0.01, the error threshold was 0.01, and the number of iterations was 100; the hidden layer of the LSTM model was 100, the learning rate was 0.001, and the regularisation parameter was 0.0001; and the sampling frequency of VMD model was 12,000, the number of samples was 2000, and the number of modes after.

VMD modal decomposition

The LSTM model is a machine learning model applicable to long time series, the return period of Sentinel-1A data is twelve days, and in this paper, a total of twenty-nine periods of data are solved, which is small for the amount of data available for training of the machine learning model. To improve the training effect of the LSTM model, the Newton interpolation method was used to interpolate the time series deformation results of PS points 3703 and 522 with an interpolation interval of one day, and three hundred and eighty-three periods of deformation sequence data with a monitoring period of one day were obtained.

The VMD model was used to perform multi-scale decomposition of the deformation sequence ($K=9$), and the nine IMF subsequences after the decomposition of PS points 3703 and 522 were shown in Fig. 6. It can be seen that the deformation sequence was decomposed by the VMD into nine IMF subsequences with different frequency scales, among which, the medium and high-frequency IMF1 ~ IMF7 subsequences are the periodic and random fluctuations present in the data, which are mainly affected by temperature, rainfall, and human engineering activities, and thus can be superimposed as disturbance terms (IMF1 + IMF2 + ... + IMF7). The

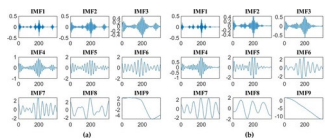


Fig. 6. VMD decomposition results ((a) PS Point 3703; (b) PS Point 522).

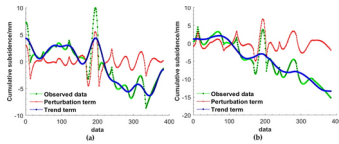


Fig. 7. Comparison of perturbation term, trend term and original deformation sequence ((a) PS Point 3703; (b) PS Point 522).

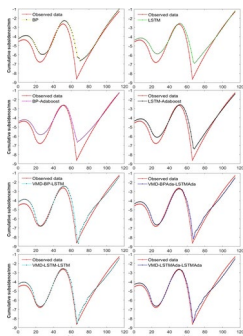


Fig. 8. Comparison of prediction results and observations for each model at No. 3703.

IMF8 and IMF9 sub-sequences in the low-frequency part are the long-term deformation trends implied in the data, which are mainly affected by the geological characteristics of the region and groundwater exploitation, and therefore can be superimposed as trend terms (IMF8 + IMF9). Comparison between the perturbation term, trend term, and the original deformation sequence data obtained by superposition after decomposition is shown in Fig. 7.

Figure 7 shows that the trend term characterizes the long-term deformation trend of PS points 3703 and 522 between 5 September 2019 and 5 October 2020, and the data series is non-smooth. The perturbation term, on the other hand, has a high degree of similarity with the original data series in terms of the deformation curve, but the shape variable fluctuates up and down around the value of zero, the cumulative shape variable varies greatly, and the data series is relatively smooth. It can also be seen that the deformation trends of the two feature points have strong similarities in the perturbation term, but are significantly different in the trend term. Among them, the overall subsidence of PS point 3703 is smaller and has leveled off in the late monitoring period, while PS point 522 continues to subside and shows an accelerated subsidence trend after the late monitoring period.

Comparison of prediction results

The BP neural network with good fitting ability to nonlinear data sequences was selected to participate in the model performance comparison and evaluation, and BP and LSTM were used as the base models, and BP-AdaBoost, LSTM-AdaBoost, VMD-BP-LSTM, VMD-BPAda-LSTMAda, and VMD-LSTM-LSTM were constructed as the comparative models, to verify the prediction performance of VMD-LSTMAda-LSTMAda based on the idea of "decomposition-prediction-combination", taking into account the fact that the summation result of the IMF components after VMD decomposition is not equal to that of the non-decomposed data, we use the original data minus the trend term as the perturbation term in the actual calculation. This can maintain the smoothness of the trend term sequence without affecting the smoothness of the perturbation term sequence, which is helpful in improving prediction accuracy and robustness. The prediction results of each model in the test set of PS points 3703 and 522 are shown in Figs. 8 and 9.

As can be seen from Figs. 8 and 9, there is a more obvious difference between the prediction results of the BP and LSTM models at the 2 feature points and the actual observations, and the BP-AdaBoost and LSTM-AdaBoost models after the integrated training have been improved, which is mainly manifested in the fact that the fit of the predicted deformation curves at the location where the deformation trend has taken a turn is improved, and the VMD-BP-LSTM and VMD-BPAda-LSTMAda models further improve the agreement between the prediction

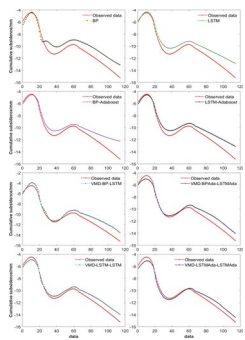


Fig. 9. Comparison of prediction results and observations for each model at No. 522.

Point	Model	RMSE/mm	MAE/mm	MAPE/%	R^2
3703	BP	5.67	0.55	10.91	0.82
	LSTM	4.46	0.45	7.72	0.86
	BP-Adaboost	4.25	0.44	7.43	0.86
	LSTM-Adaboost	3.47	0.37	6.91	0.89
	VMD-BP-LSTM	2.21	0.33	7.45	0.92
	VMD-BPAda-LSTMAda	1.05	0.29	6.87	0.93
	VMD-LSTM-LSTM	1.15	0.25	6.36	0.94
	VMD-LSTMAda-LSTMAda	0.82	0.25	6.31	0.94
522	BP	10.34	1.10	9.85	0.87
	LSTM	9.95	0.94	8.13	0.88
	BP-Adaboost	8.81	0.87	7.40	0.88
	LSTM-Adaboost	8.04	0.79	6.94	0.90
	VMD-BP-LSTM	7.43	0.73	6.82	0.91
	VMD-BPAda-LSTMAda	4.58	0.57	5.57	0.93
	VMD-LSTM-LSTM	4.46	0.56	5.40	0.94
	VMD-LSTMAda-LSTMAda	1.32	0.46	4.92	0.95

Table 3. Comparison of prediction accuracy for each model. Significant values are in bold.

results and the actual observations, showing better trend fitting ability, while the VMD-LSTM-LSTM and VMD-LSTMAda-LSTMAda models make the predicted values closer to the observed values in general, showing the global optimality of the deformation prediction.

Figure 8 shows that the turning point of the deformation trend at PS point 3703, the predicted values of the BP, LSTM, BP-AdaBoost, and LSTM-AdaBoost models are always lagging behind the actual observed values by one step, i.e., one cycle, and the deformation curves show a near-parallel phenomenon, which is not particularly obvious at PS point 522. The existence of this predicted value lagging behind the observed value by one cycle means that the prediction results will not be applied in practice and the prediction model is invalid. The VMD-BP-LSTM, VMD-BPAda-LSTMAda, VMD-LSTM-LSTM, and VMD-LSTMAda-LSTMAda models, on the other hand, attenuate the above phenomenon of prediction lag, and show a better fit at the trend turning points. Compared with the original and integrated models, reducing the non-stationarity and stochasticity of the deformed series by modal decomposition, and then using BP and LSTM models for decomposition to obtain the series prediction and combine the results can both improve the original series prediction lag and an effective way to improve the fit of the prediction curves.

Model performance evaluation

The prediction results of the eight models at two feature points were brought into the calculation of Eqs. (6) to (9), and the calculated RMSE, MAE, MAPE and R^2 values of the prediction results of the test set of deformation sequences of PS points No. 3703 and No. 522 are shown in Table 3. The statistical results of the RMSE, MAE, MAPE and R^2 values of the prediction results of the eight models for the two feature points show the same trend of the prediction accuracy, indicating that the performance differences of the eight models can be distinguished by these four indicators, which provides a reliable quantitative indicator for the evaluation of the model's performance.

Discussion

Characterisation of regional deformation along the TJHR

Figure 3 shows that the annual average deformation rate of the overall solution covering the study area ranges from -33.80 to 81.76 mm/y, with slow subsidence in general and local uplift. Figure 4 shows that the PS points where subsidence occurs are mainly concentrated in the western part of the study area near the Bianshan area and Xiaodian district, the western Bianshan area has developed agriculture and more groundwater extraction, while the rapid economic development of the Xiaodian district in recent years has led to an increase in population and a faster growth in water consumption, which is the main cause of the larger rate of subsidence in these two areas. Southeast of Qingxu extends to the western region of Jinzhong is shown as uplift, Taiyuan Basin is affected by groundwater extraction surface subsidence is serious, after many years of controlling water extraction, the subsidence trend has been effectively curbed, the effect is highlighted, in the region is shown as a trend of uplift. At the same time, it can be seen that the cumulative subsidence within the buffer 200 m on both sides of the line center line between Taiyuan South Station and Taigu East Station is -37.58 – 89.19 mm, and the annual average rate of subsidence is -26.57 – 82.63 mm/y. There exists a subsidence concentration area in the northeastern part of Jinzhong Station and the eastern side of Taiyuan Wuxu Airport, which is related to the increase of water consumption caused by the engineering construction and economic development of the area in recent years. On the other hand, there is an uplift zone north of Taigu East Station, which is located in the east of Qingxu District and the southeast of Taiyuan Xiahe Industrial Park, where the economic transformation and development has reduced the demand for agricultural water, and the groundwater has been recharged to a certain extent, resulting in the regional ground uplift, which is generally manifested as inhomogeneous subsidence.

Figure 5 shows that the deformation trend of the ten feature points exhibits slow subsidence and slow uplift, of which, No. 139 is slow uplift, while No. 207 and No. 352 show rapid uplift. Comparing with Fig. 4, it can be seen that these two points are located in the lifting area, and the PS points in this area are scarce, while the rest of the points show a trend of slow subsidence. No. 67 has the largest cumulative subsidence amount of 28.71 mm, which is located on the north side of Taigu East Station, and the subsidence trend of the area should be paid attention to continuously in the future. No. 3703 has the smallest cumulative subsidence amount of 1.29 mm, which is located in the accessory structure of Taiyuan South Station, and only on the subsidiary structure of Taiyuan South Station during the whole monitoring cycle. On the object, with large lifting and subsidence deformations occurring only on 29 September 2019, 27 March 2020, and 18 August 2020 during the entire monitoring cycle, after which it quickly returned to smoothness, and the sudden changes were random, indicating that the relative stability of the area is high. No. 522 is located on the bridge roadbed of the Jinzhong Special Bridge, which is 30.44 km long and is located at the junction of Taiyuan and Jinzhong cities, and the roadway section where No. 522 is located spans the Taiyu-an-Zhongwei-Yinchuan Railway, and is adjacent to the Datong-Xi'an High-Speed Railway to the east, and was completed from 5 September 2019 to 6 May 2020, with cumulative subsidence of 8.03 mm at No. 522, and then to the end of the monitoring on 5 October 2020, with cumulative subsidence of 15.19 mm, the cumulative subsidence under static loading is significantly higher than that during the construction period when it has not yet been put into operation, and is also related to the impact of the dynamic loading on the foundations of the neighboring Taiyuan-Zhongwei-Yinchuan Railway and the Datong-Xi'an High-speed Railway. Meanwhile, it can be seen that all the points experienced a jumping phenomenon on 27 March 2020, with the subsiding points showing rapid lifting and the lifting points showing rapid sinking, which may be related to the lifting of the datum caused by the rain and snow that occurred around that date.

Analysis of feature point deformation prediction model

The LSTM model is one of the machine learning models with excellent performance in long sequence deformation prediction, but affected by the model's limitations, the LSTM model has insufficient prediction ability in the nonlinear, non-smooth PS-InSAR monitoring deformation sequences along the high-speed railway. Figures 8 and 9 show that the LSTM prediction results lagged by one cycle compared with the observations, resulting in unavailable prediction results. Considering LSTM as a weak predictor and using the AdaBoost algorithm to construct an LSTM-AdaBoost strong predictor integrating LSTM, and repeatedly training LSTM by preset training times, Table 3 shows that the prediction accuracy is significantly improved compared with the original LSTM model, but comparing Figs. 8 and 9, it can be seen that the problem of prediction lag is not effectively solved. Meanwhile, comparing the performance of the BP model in Figs. 8, 9, and Table 3, although the prediction accuracy of the BP neural network is lower than that of the LSTM, the two models have similar prediction performance, i.e., there is also a cycle lag between the results predicted using the BP model and the observed values, and the use of the AdaBoost algorithm also improves the prediction accuracy of the BP model, but fails to eliminate the prediction lag.

VMD was usually adopted to decompose the nonlinear, non-smooth sequence data into multiple IMF sub-series, so that each IMF represents a different frequency component of the sequence data, and thus decomposes the non-smooth data sequence into a series of relatively smooth modal components. The non-linear, non-smooth feature point deformation sequence along the high-speed railway is decomposed into nine relatively smooth IMF sub-sequences using VMD, which are merged and divided into the trend term in the low-frequency part (IMF8, IMF9) and the perturbation term in the high-frequency part (IMF1 ~ IMF7) based on the frequency, and two of BP, LSTM, BPAda and LSTMAda models were selected for the prediction of the trend and the perturbation terms, respectively. The prediction results are combined into the total prediction results. Figures 8 and 9 show that the combined VMD-BP-LSTM, VMD-BPAda-LSTMAda, VMD-LSTM-LSTM, and VMD-LSTMAda-LSTMAda model predictions agree significantly better with the observations, while attenuating the effect of prediction lag on the reliability of the predictions. Table 3 further shows that the prediction accuracy of the VMD-BP-LSTM model is significantly improved over the BP, LSTM, BPAda, and LSTMAda models,

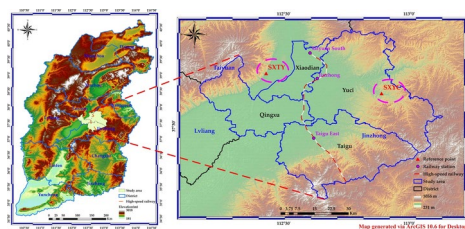


Fig. 10. Geographic map of the study area.

Number	Date	Number	Date	Number	Date
1	2019.09.05	11	2020.01.03	21	2020.05.14
2	2019.09.17	12	2020.01.15	22	2020.06.07
3	2019.09.29	13	2020.01.27	23	2020.06.19
4	2019.10.11	14	2020.02.08	24	2020.07.01
5	2019.10.23	15	2020.03.03	25	2020.07.25
6	2019.11.04	16	2020.03.15	26	2020.08.06
7	2019.11.16	17	2020.03.27	27	2020.08.18
8	2019.11.28	18	2020.04.08	28	2020.09.11
9	2019.12.10	19	2020.04.20	29	2020.10.05
10	2019.12.22	20	2020.05.02		

Table 4. Available time-series Sentinel-1A data of the study area.

while the prediction accuracy of the VMD-BPAda-LSTMAda, VMD-LSTM-LSTM and VMD-LSTMAda-LSTMAda models is significantly improved. Among them, the prediction accuracies of the VMD-BPAda-LSTMAda and VMD-LSTM-LSTM models are approximately the same, and the comparison of the evaluation indexes of each model in Table 3 shows that the prediction accuracies of the LSTM and BPAda models are also approximately the same, which suggests that the BP model can be used instead of the LSTM model to carry out the nonlinear approximate prediction of smooth sequences. The VMD-LSTMAda-LSTMAda model has the highest prediction accuracy among the four combined models (3703: RMSE = 0.82 mm, MAE = 0.25 mm, MAPE = 6.31%, R^2 = 0.94; 522: RMSE = 1.32 mm, MAE = 0.46 mm, MAPE = 4.92%, R^2 = 0.95), indicating that the "decomposition-prediction-combination" idea is an effective way to solve the nonlinear and non-stationary time series robustness.

Materials and methods

Description of the study area

Construction of the TJHR commenced on 16 June 2016 and commenced operations on 12 December 2020, spanning a total length of 358.764 km, featuring thirteen stations, and designed for speeds up to 250 km/hour³³. Notably, Taiyuan South Station, Jinzhong Station, and Taigu East Station reside within the Taiyuan Basin. Prolonged groundwater overexploitation has led to a consistent drop in groundwater levels within the basin, resulting in significant ground subsidence (Fig. 10). Despite recent efforts to regulate groundwater extraction, aquifers in the basin have witnessed effective replenishment, leading to water level rebounds and a mitigation of the ground subsidence trend. Nevertheless, heterogeneous subsidence remains a critical factor impacting large-scale construction and operations in the region. Research findings indicate that predominant ground subsidence within the Taiyuan Basin is concentrated in the central region (specifically, the Xiaodian-Qingxu-Jiaocheng-Qixian-Taigu area, with a rate of -70.0 mm/y)³². The TJHR traverses this significant subsidence zone, gradually emerging as a key threat to the railway's safe operation over time. This study focuses on Xiaodian District, Qingxu District, Yuci District, and Taigu County within the Taiyuan Basin, Shanxi Province, China, as the study area, with the TJHR segment from Taiyuan South Station to Jinzhong Station to Taigu East Station as the primary research subject.

Data sources

The twenty-nine phases of Sentinel-1A strip-mode image data covering the study area were selected for the ground subsidence deformation monitoring analysis, and each phase of data was obtained by splicing two adjacent images, with the data time-phase from 5 September 2019 to 5 October 2020, and adopting the interferometric wide swath (IW) data imaging mode, with the polarisation mode is VV + VH polarisation, the band is C-band, the spatial resolution is $5 \text{ m} \times 20 \text{ m}$ (azimuthal \times distance), the data type is Single Look Complex (SLC), the return period is 12 days, which ensures a better monitoring density, and is very advantageous for the portrayal of surface deformation features, and the reference DEM data is used to cover the image range of the SRTM 30 m data. The data acquisition time is shown in Table 4.

Technical route

Twenty-nine periods of Sentinel-1A data were firstly selected for surface deformation monitoring in the study area using PS-InSAR technology, twenty-eight issues of de-formation sequence data were acquired, and the accuracy of PS-InSAR results was verified using GNSS observation data from the continuous operation reference station of land state network; Then, ten typical PS points between Taiyuan South Station and Taigu East Station are selected as the feature points for the deformation characterisation of the research object, and one foundation point and one road base point are selected as the sample points for the training and validation of deformation prediction model; then, Newton's interpolation⁵⁰ was used to interpolate according to the interval of one day, and the three hundred and eighty-three periods deformation sequence data are obtained with one day as the monitoring period; then, the modal decomposition of deformation sequences of the two feature points was carried out using the VMD method and the results are superimposed into perturbation and trend terms according to the frequency from high to low; the LSTM model was trained with the integrated AdaBoost algorithm to obtain the LSTM-AdaBoost strong prediction model; the LSTM-AdaBoost model was then used to predict the perturbation terms and trend terms respectively, and the two predictions were combined as the prediction of deformation in the feature points; Finally, the prediction accuracy of the model was evaluated to achieve the deformation monitoring and prediction along the high-speed railway. The specific steps are as follows (Fig. 11):

- (1) Acquire Sentinel-1A data and DEM data covering the study area, carry out PS-InSAR solving to obtain the deformation sequence of the study area, transform the subsidence along the line-of-sight direction to the vertical direction, and verify the accuracy of the InSAR results by using the GNSS observation data from the SXTY station of the land-state network.
- (2) Ten typical PS points in the 200 m buffer zone on the left and right sides of the research object are selected as feature points, and these feature points are used to characterize the deformation of the research area and the research object, and the de-formation sequence of one feature point located on the foundation and one located on the roadbed are selected as the data source for the subsequent experiments.
- (3) Interpolate the experimental data with Newton's interpolation method with an interpolation interval of one day to obtain the deformation sequences with equal time intervals, and divide the first 70% of the deformation sequences as the training set of the prediction model, and the last 30% as the test set.
- (4) Input the deformation sequences into the VMD model for modal decomposition, and set the modal number to nine to obtain the subsequence IMF1 ~ IMF9, super-impose the summation results of IMF1 ~ IMF7 as the perturbation term, and the summation results of IMF8 and IMF9 as the trend term.
- (5) The AdaBoost algorithm is used to integrate and train the LSTM model, and the trained LSTM-AdaBoost model is used to predict the perturbation term and trend term obtained from VMD decomposition respectively, and the combination of the above two prediction results as the final prediction result is adopted in an equally weighted way, to establish the VMD-LSTMAda-LSTMAda model for the prediction of deformation along the high-speed railway. Model.
- (6) The model prediction accuracy was evaluated using Root Mean Squared Error (RMSE), Mean Absolute Error (MAE), Mean Absolute Percentage Error (MAPE), and Coefficient of Determination (R^2), and BP-AdaBoost, LSTM-AdaBoost, VMD-BP-LSTM, VMD-BPAda-LSTMAda and VMD-LSTM-LSTM models were constructed based on BP and LSTM models for comparative analyses of VMD-LSTMAda-LSTMAda model performance and its applicability.

PS-InSAR technology

PS-InSAR technique uses $N + 1$ SAR images of the same area, selects one of them as the main image, and the remaining N images as the auxiliary images, and makes a difference with the phase values of the corresponding pixels of the permanent scatterers (e.g. buildings, bridges, roads, etc.) of the main image, respectively, to obtain N differential interferograms. The residual topography, target offset, and atmospheric effects are calculated by selecting high-quality feature points as permanent scatterer points (PS points), and the surface deformation is inverted according to the linear model. where the phase φ_i of i differential interferogram is Ref.⁴⁹:

$$\varphi_i = \phi_{def_i} + \phi_{topo_i} + \phi_{flat_i} + \phi_{atm_i} + \phi_{noise_i} \quad (2)$$

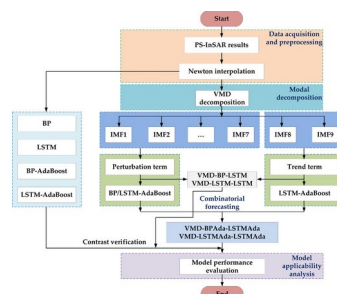


Fig. 11. The general technology roadmap of this study.

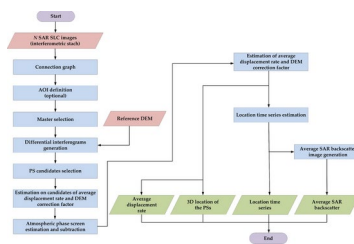


Fig. 12. Flow chart of PS-InSAR technology.

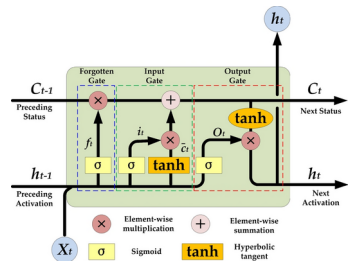


Fig. 13. Schematic diagram of LSTM network structure.

where, ϕ_{def_i} is the deformation phase in the LOS direction; ϕ_{topo_i} is the residual terrain phase; ϕ_{flat_i} is the horizon; ϕ_{atm_i} is the atmospheric delay phase; ϕ_{noise_i} is the phase of other noise.

As shown in Fig. 12, the PS-InSAR technology could process the acquired deformation variables up to the millimeter level, and when monitoring the regional subsidence along the high-speed railway, it can selectively screen the typical PS points along the characteristic areas, obtain the continuous and reliable deformation sequences, and then analyze the de-formation characteristics and predict the deformation trend.

Long short-term memory network (LSTM)

LSTM is indeed a variant of recurrent neural networks designed to address the challenges of the gradient explosion or vanishing problem encountered in simple recurrent neural networks. The key innovation of LSTM lies in its introduction of the Gating Mechanism, which effectively regulates the flow of information within the network. The formula for these three gates:

$$f_t = \sigma(W_f \cdot [h_{t-1}, A_t] + b_f) \quad (3)$$

$$i_t = \sigma(W_i \cdot [h_{t-1}, A_t] + b_i) \quad (4)$$

$$o_t = \sigma(W_o \cdot [h_{t-1}, A_t] + b_o) \quad (5)$$

where, W_f, W_i, W_o are the weight matrices of the forgetting gate, the input gate, the current input cell, and the output, respectively. b_f, b_i, b_o are the bias terms for the oblivion gate, the input gate, the current input cell, and the output respectively. $[h_{t-1}, A_t]$ means that two vectors are joined into a longer vector. σ is the Sigmoid function.

The LSTM network structure is shown in Fig. 13³⁵, which is computed as follows:

The three gates (forget gate, input gate, and output gate) are computed based on the external state h_{t-1} from the previous time step, the input X_t at the current time step, and the candidate state \bar{c}_t .

The forgetting gate f_t and the input gate i_t work together to update the memory cell c_t .

The output gate o_t combines information from the internal state and passes it to the external state h_t .

Model evaluation

In assessing the performance of the prediction model, metrics such as RMSE, MAE, MAPE, and R^2 were selected as the evaluation indices. A decrease in the values of RMSE, MAE, and MAPE signifies enhanced accuracy in model predictions and an overall improvement in the prediction model. Conversely, R^2 , within the [0,1] range, serves as a gauge of the model's predictive capability; the closer R^2 approaches 1, the stronger the model's predictive ability, and vice versa. The formulae for each evaluation indicator are set out below:

$$RMSE = \sqrt{\frac{1}{N} \sum_{i=1}^N (x_i - \hat{x}_i)^2} \quad (6)$$

$$MAE = \frac{1}{N} \sum_{i=1}^N \left| x_i - \hat{x}_i \right| \quad (7)$$

$$MAPE = \frac{1}{N} \sum_{i=1}^N \left| \frac{x_i - \hat{x}_i}{x_i} \right| \times 100\% \quad (8)$$

$$R^2 = 1 - \frac{\sum_{i=1}^N (x_i - \hat{x}_i)^2}{\sum_{i=1}^N (x_i - \bar{x}_i)^2} \quad (9)$$

where, N is the sample size, $x_i (i = 1, 2, \dots, N)$ is an observation, \hat{x}_i is the predicted value of x_i and \bar{x} is the mean of x_i .

Conclusions

The Taiyuan Basin has been affected by groundwater mining leading to significant surface subsidence, which poses potential risks to the safe operation of high-speed railways, highways, and other linear projects operating in the basin. Based on the PS-InSAR technique, the surface subsidence results of the area along the TJHR in the study area within one year before the completion and operation were obtained, the subsidence characteristics of ten PS points along the line were analyzed, and the de-formation prediction of two of these feature points was carried out by using the VMD-LSTMAda-LSTMAda model. The results show that:

- (1) The overall subsidence trend in the study area shows uplift in the southwest, subsidence in the northwest, and smooth in the east, and the surface subsidence between Taiyuan South Station and Taigu East Station shows uneven subsidence in general, and the exploitation of groundwater for industrial and agricultural production and people's life is the main driving force leading to the development of ground subsidence in the area, which poses a potential threat to the subsequent healthy operation of TJHR in the context of the control of groundwater exploitation in Taiyuan City.
- (2) The AdaBoost algorithm can improve the prediction accuracy of BP and LSTM models on nonlinear and nonsmoothed sequences, but it can't effectively eliminate or weaken the prediction lag problem caused by the constant change of the trend of the deformation sequence, and the prediction results with prediction cycle lag are of no practical value in production.
- (3) The VMD decomposition reduces the complexity of the deformation sequence along the high-speed railway, the sub-sequences are smoother than the original sequence, the AdaBoost integrated training improves the prediction accuracy of the LSTM model, and the combined LSTMAda model gives fuller play to the advantages of the LSTM model in the prediction of the sequence data, therefore, the VMD-LSTMAda-LSTMAda model can obtain more accurate and robust prediction results.
- (4) PS-InSAR technology has the problem of insufficient identification of PS points in the outskirts of towns and rural areas, while interpolation will lead to the amplification of the sedimentation rate in the blank area of PS points, which affects the accuracy of the analysis of the extreme value of sedimentation, and in the future, we should try to use the SBAS-InSAR technology for sedimentation monitoring. Meanwhile, there is a certain subjectivity in combining the IMF subseries after deformation time series de-composition into disturbance and trend terms, and in the future, we should consider combining each IMF subseries with equal weights after predicting them separately, to improve the objectivity and automation of the process.

Data availability

The datasets used and/or analyzed during the current study are available from the corresponding author on reasonable request.

Received: 26 March 2024; Accepted: 14 October 2024

Published online: 19 October 2024

References

1. Li, Q. et al. A novel track measurement system based on GNSS/INS and multisensor for high-speed railway. *Acta Geod. Cartogr. Sin.* **5**, 569–579 (2020).
2. Meng, X. G. Application of closed loop attachment leveling in Beijing-Shanghai high-speed railway. *Bull. Surv. Map.* **S1**, 202–204 (2012).
3. Wang, J. H. Discussion on application of total station for observation of subsidence of piers in water of a high speed railway bridge. *Railway Investig. Surv.* **5**, 9–12 (2011).
4. Gao, Z. F. Automatic monitoring technology for track geometry conditions in subgrade deformation section of operating high speed railway. *Railway Eng.* **7**, 137–141 (2018).
5. Feng, B. Q., He, H., Li, C. X., Yang, F. Y. & Sun, G. Q. Deformation monitoring method of railway communication tower based on GNSS. *Railway Eng.* **9**, 154–158 (2020).
6. Yang, H. et al. The study of hydrostatic levelling system applying in high-speed railway operating period to real-time monitoring settlement. *Railway Investig. Surv.* **6**, 28–31 (2015).

7. Hua, Y. Y., Hu, J. S., Kang, J. R. & Xu, J. Study on the law of surface subsidence with multiple working faces in daning mining area based on SBAS-DInSAR. *Met. Min.* **3**, 177–183 (2020).
8. Gao, M. et al. InSAR time-series investigation of long-term ground displacement at Beijing Capital International Airport. *Tectonophysics* **691**, 271–281 (2016).
9. Ye, G.H. et al. Application of airborne LiDAR technology in dune deformation monitoring. *Laser Optoelectron. P.* **5**, 394–401 (2018).
10. Wang, W., Dang, Y. M., Zhang, C. Y. & Yang, Q. Application of CORS network and GNSS technology in ground deformation monitoring: Taking southeast Zhejiang Province as an example. *Chin. J. Geol. Hazard Control.* **2**, 73–77 (2021).
11. Meng, W. L., Cai, L. L., Yang, W. S. & Wang, S. S. Mining subsidence prediction method based on geomagic. *Met. Min.* **1**, 126–131 (2017).
12. Liu, S. L., Zhang, D., Zhang, P. S., Wang, J. C. & Shi, B. Deformation monitoring of overburden based on distributed optical fiber sensing. *J. Eng. Geol.* **6**, 1118–1125 (2016).
13. Xing, X. M. et al. Detecting the regional linear subsidence based on CRInSAR and PSInSAR integration. *Chin. J. Geophys.* **5**, 1193–1204 (2011).
14. Zhang, X. Q., Xie, R. G., Dai, W. J., Zhou, Y. H. & Kuang, C. L. Research and realization of high spatiotemporal resolution ground subsidence monitoring system. *Bull. Surv. Map.* **7**, 68–71 (2015).
15. Falk, A., Galloway, D. L., Bell, J. W., Zebker, H. A. & Laczniak, R. J. Sensing the ups and downs of Las Vegas: InSAR reveals structural control of land subsidence and aquifer-system deformation. *Geology* **6**, 483–486 (1999).
16. Hu, F. et al. Monitoring deformation along railway systems combining multi-temporal InSAR and LiDAR data. *Remote Sens.* **11**, 2298 (2019).
17. Dong, J. J., Li, X., Mei, Y. & Liu, S. Y. D-InSAR monitoring of site stability for surface substation above old mine goaf. *J. Min. Saf. Eng.* **1**, 62–71 (2022).
18. Liu, H. et al. Application of DInSAR technology in vertical deformation monitoring of subgrade and slope in Chengdu-Kunming double track railway. *Railway Eng.* **3**, 67–72 (2020).
19. Yang, B. et al. Ground subsidence monitoring and time-series evolution situation analyzing along high speed railway in Beijing-Tianjin-Hebei region. *China Railw. Sci.* **1**, 1–9 (2020).
20. Ferretti, A., Prati, C. & Rocca, F. L. Permanent scatterers in SAR interferometry. *IEEE Trans. Geosci. Remote Sens.* **1**, 8–20 (2001).
21. Ma, F. H., Jiang, S. S. & Sun, C. Y. Application of PS InSAR in monitoring land subsidence in Yanshan mining area. *J. Appl. Sci.* **6**, 969–977 (2018).
22. Wei, J. C., Zhang, H. X., Bai, Z. C. & Wang, S. Q. Integrated monitoring method of the mining subsidence of Shendong mining area based on D-InSAR and PS-InSAR technology. *Met. Min.* **10**, 55–60 (2019).
23. Wei, C. M., Ge, W. P., Shao, Y. X. & Wu, D. L. Surface deformation field of Eastern Gansu province by PS-InSAR technique with sentinel-1A. *Remote Sens. Technol. Appl.* **4**, 864–872 (2020).
24. Fan, H. D., Deng, K. Z., Zhu, G., Chen, B. G. & Li, P. X. Deformation monitoring and prediction methods for expressway above goaf based on time series SAR technique. *J. Chin. Coal Soc.* **11**, 1841–1846 (2012).
25. Liu, Q. et al. Temporal and spatial characteristics analysis of deformation along Foshan subway using time series InSAR. *Geomat. Inform. Sci. Wuhan Univ.* **7**, 1099–1106 (2019).
26. Ren, C. et al. Land subsidence detection and analysis along subway based on sentinel-1A time series interferometry synthetic aperture radar. *Sci. Technol. Eng.* **2**, 803–808 (2020).
27. Ge, L. L. et al. Impact of ground subsidence on the Beijing-Tianjin high-speed railway as mapped by radar interferometry. *Geogr. Inf. Sci.* **2**, 91–102 (2010).
28. You, H. et al. Monitoring and prediction of subsidence along high speed railway supported by InSAR technology. *Sci. Surv. Map.* **7**, 67–75 (2021).
29. Zhu, W. et al. Recent ground deformation of Taiyuan basin (China) investigated with C-, L-, and X-bands SAR images. *J. Geodyn.* **70**, 28–35 (2013).
30. Zhang, Q. et al. Two-dimensional deformation monitoring over Qingxu (China) by integrating C-, L- and X-bands SAR images. *Remote Sens. Lett.* **1**, 27–36 (2014).
31. Liu, Y. Y. et al. Land subsidence in Taiyuan, China, monitored by InSAR technique with multisensor SAR datasets from 1992 to 2015. *IEEE J. Sel. Top. Appl. Earth Obs. Remote Sens.* **11**, 1509–1519 (2018).
32. Tang, W. et al. Monitoring land subsidence by time series InSAR and wavelet analysis of seasonal deformation in Taiyuan Basin. *Chin. J. Geophys.* **6**, 2352–2369 (2023).
33. Qiu, D. et al. Land subsidence analysis along high-speed railway based on EEMD-Prophet method. *Sci. Rep.* **1**, 1–17 (2024).
34. Hochreiter, S. & Schmidhuber, J. Long short-term memory. *Neural Comput.* **8**, 1735–1780 (1997).
35. Du, C., Zu, F. J. & Han, C. P. Approach to predict land subsidence in old goafs considering the influence of engineering noise. *Shock Vib.* **3831441**, 1–13 (2022).
36. Tang, Y. F., Hu, G. Z. & Zhou, S. A. Displacement prediction of sudden landslide based on dynamic residual correction LSTM algorithm. *Chin. Saf. Sci. J.* **8**, 109–116 (2023).
37. Chen, Z. A., Xiong, X. & You, Y. Y. Variational mode decomposition and long short time neural netw Variational mode decomposition and long short time neural network for dam deformation prediction. *Sci. Surv. Map.* **9**, 34–42 (2021).
38. Ye, Y., Yan, C., Luo, X., Zhang, R. & Yuan, G. Analysis of ground subsidence along Zhengzhou metro based on time series InSAR. *Natl. Remote Sens. Bull.* **26**, 1342–1353 (2022).
39. Pan, H. Y., Zhao, Y. H., Zhang, W. D., Bai, Y. & Han, Y. W. Prediction of surface subsidence with improved BP neural network based on AdaBoost. *Coal Sci. Technol.* **2**, 161–167 (2019).
40. Meng, X. W., Tang, J. J. & Wang, Z. Trajectory prediction of vehicles based on LSTM-AdaBoost model considering lane-changing intention. *Comput. Eng. Appl.* **13**, 280–287 (2022).
41. Ni, W., Zhao, L., Zhang, L., Xing, K. & Dou, J. Coupling progressive deep learning with the adaboost framework for landslide displacement rate prediction in the Baihetan dam reservoir, China. *Remote Sens.* **15**, 2296 (2023).
42. Dragomiretskiy, K. & Zosso, D. Variational mode decomposition. *IEEE Trans. Signal Process.* **3**, 531–544 (2014).
43. Wang, C. H., Zhao, Y. J., Guo, W., Meng, Q. J. & Li, B. Displacement prediction model of landslide based on ensemble empirical mode decomposition and support vector regression. *Acta Geod. Cartogr. Sin.* **10**, 2196–2204 (2022).
44. Meng, Q. C. et al. Combined prediction model of bridge deformation response based on EEMD-LSTM. *J. Chongqing Jiaotong Univ. (Nat. Sci.)* **5**, 25–34 (2023).
45. Wang, Z. H., Nie, W., Xu, H. H. & Jian, W. B. Prediction of landslide displacement based on EEMD-prophet-LSTM. *J. Univ. Chin. Acad. Sci.* **4**, 514–522 (2023).
46. Yang, G. L., Yu, H. S. & Huang, C. PM2.5 concentration prediction based on optimization combination model. *Comput. Eng. Des.* **10**, 3132–3137 (2023).
47. Qi, J. X., Su, X. L., Zhang, G. X. & Zhang, T. Research on monthly runoff prediction of VMD-LSTM model in different forecast periods. *Agric. Res. Arid. Areas* **6**, 258–267 (2022).
48. Chen, H., Lu, T., Huang, J., He, X. & Sun, X. An improved VMD-EEMD-LSTM time series hybrid prediction model for sea surface height derived from satellite altimetry data. *J. Mar. Sci. Eng.* **11**, 2386 (2023).
49. Wang, L., Zhou, C., Gong, H., Chen, B. & Xu, X. Land subsidence prediction and analysis along typical high-speed railways in the Beijing-Tianjin-Hebei Plain area. *Remote Sens.* **15**, 4606 (2023).

50. Xue, Y. A., Ji, Z. & Zhang, W. Z. Study on residual deformation prediction of goaf based on residual modified GM(1,1)model. *Safe Coal Min.* **1**, 101–108 (2023).

Acknowledgements

This research was funded by Shanxi Coal-Based Low-Carbon Joint Fund Key Project of National Natural Science Foundation of China, grant number U1810203 and U22A20620, the Ministry of Education Industry-University Collaborative Education Funding Project, grant number 202102245009 and 22087106262449. We thank the First Monitoring and Application Center, China Earthquake Administration for providing the GNSS velocity field datasets/ time series of GPS stations.

Author contributions

All of the authors made significant contributions to this study. Conceptualization, Y.X. and Y.Z.; Methodology, Y.X. and Y.Z.; Validation, Y.X.; Formal Analysis, Y.X. and W.Z.; Data Curation, Y.X. and H.L.; Resources, Y.X. and H.L.; Writing-Original Draft Preparation, Y.X.; Writing-Review & Editing, Y.X.; Supervision, Y.X.; Funding Acquisition, Y.Z and W.Z. All authors have read and agreed to the published version of the manuscript.

Declarations

Competing interests

The authors declare no competing interests.

Additional information

Correspondence and requests for materials should be addressed to Y.-A.X.

Reprints and permissions information is available at www.nature.com/reprints.

Publisher's note Springer Nature remains neutral with regard to jurisdictional claims in published maps and institutional affiliations.

Open Access This article is licensed under a Creative Commons Attribution-NonCommercial-NoDerivatives 4.0 International License, which permits any non-commercial use, sharing, distribution and reproduction in any medium or format, as long as you give appropriate credit to the original author(s) and the source, provide a link to the Creative Commons licence, and indicate if you modified the licensed material. You do not have permission under this licence to share adapted material derived from this article or parts of it. The images or other third party material in this article are included in the article's Creative Commons licence, unless indicated otherwise in a credit line to the material. If material is not included in the article's Creative Commons licence and your intended use is not permitted by statutory regulation or exceeds the permitted use, you will need to obtain permission directly from the copyright holder. To view a copy of this licence, visit <http://creativecommons.org/licenses/by-nc-nd/4.0/>.

© The Author(s) 2024